Smarter cell sorting: droplet microfluidics meets pick-and-place sorting

Olivia Gerhard, Steffen Schneider, Michaela Dehne, Janina Bahnemann, Klaus Palme, Ralf Welsch, Oleksandr Dovzhenko, Qiuju Yu, Michael Köhler, Jialan Cao, Alexander Groß

Angaben zur Veröffentlichung / Publication details:

Gerhard, Olivia, Steffen Schneider, Michaela Dehne, Janina Bahnemann, Klaus Palme, Ralf Welsch, Oleksandr Dovzhenko, et al. 2025. "Smarter cell sorting: droplet microfluidics meets pick-and-place sorting." Lab on a Chip. https://doi.org/10.1039/d5lc00550g.

Lab on a Chip

PAPER

View Article Online
View Journal

Cite this: DOI: 10.1039/d5lc00550g

Smarter cell sorting: droplet microfluidics meets pick-and-place sorting

Olivia Gerhard, [a] Steffen Schneider,[a] Michaela Dehne, [bc] Janina Bahnemann, [bd] Klaus Palme, [ef] Ralf Welsch, [e] Oleksandr Dovzhenko, [e] Qiuju Yu, [e] Michael Köhler, [a] Jialan Cao *[a] and Alexander Groß *[a]

Single-cell manipulation based on image-derived selection criteria is essential for morphology-based screening applications. This requires a fast and robust 'pick-and-place' technology to single-out the identified hits from the rest of the population. However, the overall efficiency of this process is influenced by several parameters, primarily constrained by the limitation of moving only one target at a time per cycle. To overcome this bottleneck, we present a system that employs a microfluidic droplet-based approach, enabling the sequential transfer of multiple objects in each cycle. The core of this system is the microfluidic transfer tool (MTT), which enables selected cells to be sequentially 'picked' and encapsulated into individual nanoliter-scale droplets. The resulting droplet sequence serves as a temporary storage buffer for the picked objects before they are transferred to a designated target. Here, hit-containing droplets can be individually 'placed' requiring just one global movement from source to target. To demonstrate the applicability of this approach, the developed MTT was integrated into an experimental robotic environment. Fluorescent particles of about 45–63 μm diameter and different colors were used to benchmark the system. This sequential microfluidic processing resulted in an overall performance improvement by a factor of approximately 20 compared to traditional single-object pick-and-place techniques. Detailed information about the MTT design and the overall workflow are provided.

Received 4th June 2025,
Accepted 13th October 2025

DOI: 10.1039/d5lc00550g

rsc.li/loc

Introduction

High-content screening including morphology-based or phenotype-based information has become an essential approach in the field of drug discovery and cell line development.[1–6] This methodology utilizes microscopic imaging combined with advanced image analysis algorithms to detect subtle differences in the shape, size, and structural characteristics of living cells or cellular objects. Traditional image analysis requires typically bright field or fluorescence imaging as readout parameters. Here, live-cell staining is essential for image-based extraction of structural features for classifying cells by morphology.[7–9] If cell lines with reporter gene expression are available, the expression of fluorescent proteins can also be analysed by imaging.[10,11] From a biological perspective, morphological criteria have long been the standard for monitoring cell development and optimizing incubation conditions. The advantages of morphology-based screening are especially significant in plant biotechnology, where examining morphological differentiation of cellular structures is crucial for identifying rare hits. The identification process often hinges on analysing subtle morphological changes, which may indicate successful transformations or mutations.[12] Despite numerous benefits, image-based techniques possess challenges, including the demands for reliable optical data acquisition, management of image data formats, and algorithmic decision-making based on image analysis.

Accurate decision-making relies on high-quality, consistent imaging, which depends not only on the camera system but also—critically—on optimized illumination for revealing fine structural features. Once assay criteria and optical evaluation are established, the next important step is sorting the identified hits from the remaining population. Therefore, an efficient pick-and-place system is required for a careful selection of sensitive objects. An alternative approach to selectively picking

[a] Institute for Chemistry and Biotechnology, Chair Physical Chemistry and Microreaction Technology, Technische Universität Ilmenau, 98693 Ilmenau, Germany. E-mail: jialan.cao@tu-ilmenau.de, alexander.gross@tu-ilmenau.de
[b] Institute of Physics, Chair Technical Biology, University of Augsburg, 86159 Augsburg, Germany
[c] Institute of Technical Chemistry, Leibniz University Hannover, 30167 Hannover, Germany
[d] Centre for Advanced Analytics and Predictive Sciences (CAAPS), University of Augsburg, Germany
[e] ScreenSYS GmbH, 79108 Freiburg, Germany
[f] BIOSS Centre for Biological Signalling Studies, University of Freiburg, 79104 Freiburg, Germany

only the "cherries" is to isolate single hits using the limited-dilution technique based on stochastic principles. This straightforward but effective method isolates individual cells by pipetting small aliquots from a diluted cell mixture into multiple containers. However, since cell distribution follows a Poisson distribution, achieving true single-cell resolution requires high dilution steps and many aliquots, increasing the experimental demands and necessitating meticulous monitoring.[13–15] For example, isolating single cells from a mixture containing 1000 cells ml^{-1} requires preparing around 6712 aliquots per ml to ensure a 99% probability of obtaining at least one cell per aliquot (see SI). Consequently, 5782 (86%) of the aliquots are empty and only about 860 single occupied. To streamline this process, pooling and pre-selecting mixtures before isolating individual hits can reduce the number of data points involved. However, producing several sets of approximately 100 objects each — identifying the batch containing the hit, and then isolating the final 100 — necessitates multiple pipetting steps, increasing the risk of missing the hit, particularly during detailed morphological analyses. Both approaches are time-consuming and resource-intensive compared to a pick-and-place strategy, especially in selection campaigns with low hit rates, such as 1 in 10 000, which require a performant pick-and-place technology to efficiently "harvest only the cherries."

While pick-and-place systems are widely available, they are limited in throughput. A typical pick-and-place process operates in repetitive automated loops, involving optical identification, decision-making, positional adjustments, object capture, transfer to target positions, and verification. The movement between source and target for each transfer is particularly most time-consuming step, with commercial systems typically achieving a cycle time of around 30 seconds per object.[16–19]

To enhance the efficiency of pick-and-place processes, we developed a microfluidic transfer tool (MTT) which makes use of droplet-based intermediate storage to transfer multiple selected objects in a single cycle. A fully operational pick-and-place workflow requires both imaging and robotic support. The applied workflow, including images of the key features, is presented in Fig. 1. Currently, key motivation for applying droplet microfluidics in screening is its ability to

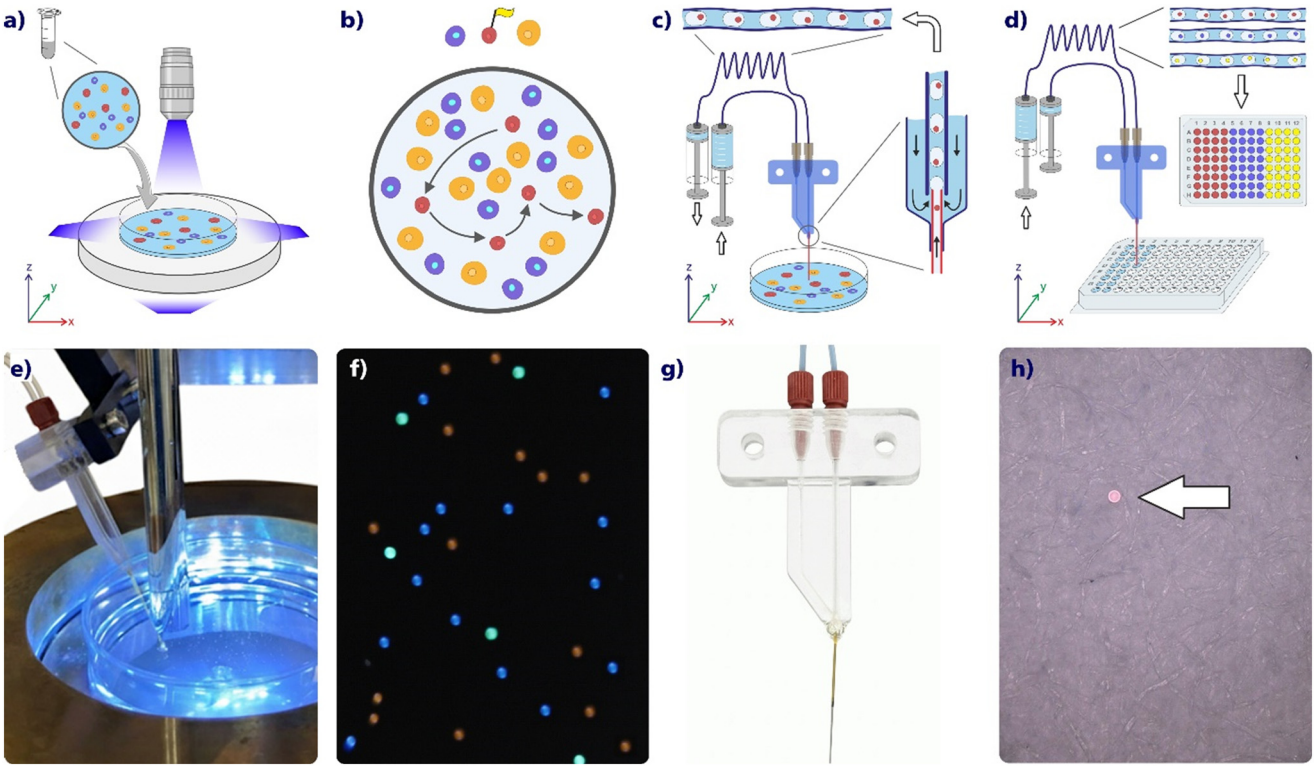

Fig. 1 Improved morphology-based objects sorting process using intermediate droplet storage. This scheme and belonging images visualize the required subsequent operational steps to classify objects by image-based sorting. a) Sample preparation and imaging optimization: careful adjustment of the excitation conditions to ensure optimal object spacing and imaging quality. b) Image analysis and hit identification: the system automatically identifies target hits and their locations based on morphological criteria and plan the pickup order accordingly. c) Sequential picking and droplet storage: using the microfluidic transfer tool – MTT all identified hit objects are picked up and encapsulated into individual droplets for intermediate storage. d) Sequential Placement & hit separation: each individual droplet from the stored droplet sequence bearing the encapsulated objects will be dispensed into an individual well or designated surface location. Image shows a polymeric object placed on a wicking paper surface. All positional movements are executed by *x,y,z*-robotic support (details see Text and SI). e) Image of the developed excitation setup showing object excitation in the Petri dish. f) Image of differently colored polymer particles between 40–60 μm diameter for sorting. g) 3D-printed microfluidic-transfer-tool (MTT) equipped with capillary and fluidic connectors. h) Image of a singled-out 50 μm bead on a wicking paper surface after sequential transfer.

process low sample volumes at high number throughput.[20–22] Droplet microfluidic systems show great potential in biological and biochemical assays as well as in the chemistry field.[23–27] But, droplet-based microfluidics has emerged as a powerful platform for high-throughput cell sorting as well. By encapsulating entire cell populations into thousands of single-cell droplets through a microfluidic emulsification step, the handling and manipulation of single-cells becomes less demanding, as they can be sorted[28–31] and analysed at the level of the pico- or nano-litre droplet scale.[32] In this way high sorting rates of about kHz (ref. 33 and 34) can be achieved if the decision making process bases on spectral readouts.[35,36] The effort required for sorting droplet-encapsulated objects increases accordingly when using image-based decisions.[37] Performing detailed optical analysis of cell morphology within small droplets remain challenging. In this context, the pick-and-place approach offers advantages due to enhanced optical accessibility. However, the morphology-based screening of plant cell cultures for the development of embryogenic structures from haploid microspore stem cells in droplets was previously demonstrated by us.[12] The future application of the fluidic sorting approach presented here could significantly support such plant cell developments. Another microfluidic approach for selective cell translocation was described by V. Zieger *et al.* In this system, cells (organoids) were taken up into a tube connected to a piezo dispenser. The resulting pick–flow–drop setup enabled image-controlled positioning at the tube's inlet side as well as localized dispensing at the piezo outlet side.[38]

The application of microfluidic devices depends strongly on the compatibility of the intended process with the selected device materials. In addition to chemical material stability, biocompatibility typically represents the most critical factor. The required microstructural features—such as channel diameters or junction dimensions—are further constrained by the limitations of the used manufacturing technique. Developing microfluidic devices from silicon or glass involves complex processes such as lithography, etching, and packaging, which constrain both adaptability and design flexibility.[39,40] The utilization of polymeric materials in the development of microfluidic devices is primarily dictated by considerations of material compatibility and the complex fabrication techniques required for producing single units or small batches.[39] Here, recent advancements in three-dimensional printing (3DP) technologies have driven different application possibilities for polymer microfluidic components.[40–42] Techniques such as PolyJet printing enable the fast formation of high-resolution 3D fluidic devices using different materials in a very efficient way. This facilitates the creation of intricate microfluidic systems, such as cell separators, and unlocks new application opportunities, including the potential use in tissue engineering-based microfluidics.[41,45] Hence, PolyJet printing was employed for the development and optimization of the MTT.

Ultimately, a fused-silica capillary and a PTFE-tubing were integrated into the 3D-printed frame to meet all compatibility and functional requirements. The MTT facilitates droplet encapsulation to temporarily store the subsequently picked objects in a droplet sequence before their transfer and individual placement. This procedural workflow which can pickup and place a plurality of hit objects in one operational passage saves time because multiple movement operations between source and target are saved. This microfluidic approach significantly accelerates pick-and-place sorting, supporting efficient morphology-based screening approaches.

Experimental

The microfluidic transfer tool (MTT)

Fig. 2 shows the MTT including flow-scheme and structural details. The core function of the MTT is to sequentially pickup multiple objects and to store them temporarily as a droplet sequence before transferring the individual droplets onto a target platform. This process involves the selective aspiration of desired objects including their aqueous medium followed by compartmentalization into individual droplets by interspacing the aqueous stream with fluorinated oil, thereby generating a regular droplet sequence (see Fig. 2b). Fluorinated oil is the material of choice because it is immiscible with water, chemically inert, and exhibits negligible extraction properties. Its high oxygen permeability is essential for maintaining the viability of living, oxygen-sensitive cells during processing and intermediate storage. When combined with PTFE tubing, which also provides significant gas permeability, this setup creates a proven environment for both long time incubation as well as intermediate storage of droplet-encapsulated cells.[43] Since the aspirated objects are suspended in aqueous media, proper compartmentalization requires an appropriate fluidic junction inside the microfluidic device for proper droplet formation. Accordingly, three fluid streams must be controlled inside the device: the outflow rate Q_{out}, which drives aspiration into the storage tubing; the inflow rate Q_{in}, which supplies fluorinated oil for fluidic compartmentalization; and the effective uptake flow Q_{takeup}, which is ultimately responsible for object acquisition (see Fig. 2b). Both Q_{out} and Q_{in} were controlled by precision syringe pumps operating in opposite directions, while Q_{takeup} results from the difference between these two flowrates. To get a stable and reproducible droplet formation, the aspirated aqueous stream Q_{takeup} must be combined with the fluorinated oil stream Q_{in} in a manner that enables the generation of regular droplets with constant volume. To minimize sensitivity to flow rate variations while maintaining both stability and reproducibility, circular cross-flow geometry with radial oil injection was chosen (see Fig. 2b).

For fluid actuation the syringe pump and the MTT were connected using standard OD = 0.8 mm PTFE tubing with an inner diameter of 0.5 mm, secured by appropriate fluidic fittings. As part of the initialization routine, all syringes, tubing, and the MTT have to be primed bubble-free with the fluorinated oil. The microfluidic device was fabricated using high-resolution ProJet MJP 2500 Plus 3D-printer. The biocompatible polyacrylate VisiJet M2S-HT90 was used as the printing material, while the heat-labile VisiJet M2 SUP served

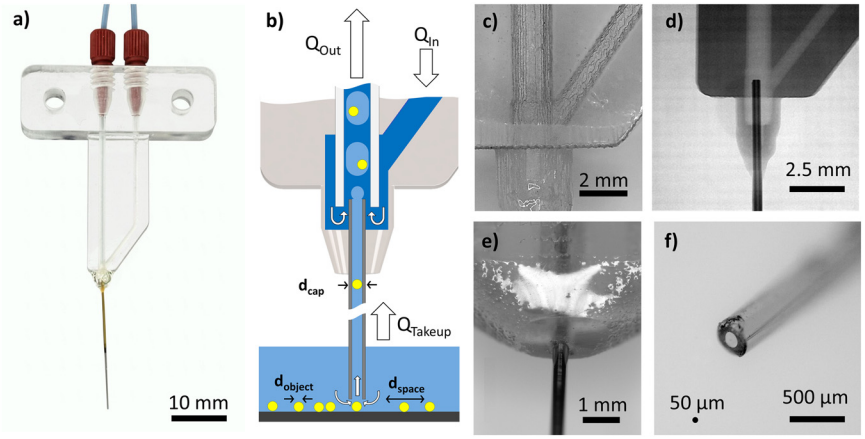

Fig. 2 Microfluidic transfer tool (MTT) design and images. a) The image shows the 3D-printed MTT including the embedded 20 mm long fused silica capillary, featuring an outer diameter (OD) of 360 µm and an inner diameter (ID) of 100 µm. b) The scheme shows the operational principle of the MTT including the droplet forming junction while embedding aspirated objects into a droplet sequence. The capillary tip has to be immersed into medium containing various submerged objects for sorting. The aspiration flow rate (Q_{takeup}) produces a fluidic force that draws in non-adherent, targeted objects into the capillary. To aspirate a sequence of optically selected target-objects, the tip must be maneuvered sequentially over each desired target without inadvertently aspirating non-target objects. For effective single object selection, the spacing between objects (d_{space}) and capillary diameter (d_{cap}) must be considered to maximize single-pick efficiency. Once aspirated, the objects are guided through the capillary and subsequently encapsulated into droplets at a co-flow junction. Here, the aspirated aqueous medium (Q_{takeup}) merges with the fluorinated oil (Q_{in}). The junction is formed by positioning the upper capillary side within the PTFE tubing. This configuration enables stable and reproducible droplet generation directly inside the PTFE tubing, where the droplets are temporarily stored before being dispensed to the target location. c) The image shows details of the 3D-printed MTT indicating printing layers inside the channel structure. The exterior surface has been coated with a lacquer to enhance the level of transparency. d) The X-ray image shows the droplet forming junction, highlighting the capillary's end and its design to accommodate the PTFE tubing. The light parts indicate the fluidic channels. e) Image of the interface of the fused-silica capillary to the MTT showing the capillary inserted into the MTT. f) Image of the capillary tip, featuring a scale indicator for a 50 µm diameter object.

as the support material.[44] The device was printed in a horizontal orientation to achieve the highest printing resolution along their longitudinal axis. In Fig. 2c the printing layers along the inner channels can be recognized.

The fluorinated oil is introduced *via* a supporting channel leading to the droplet formation junction. However, the stability of droplet sequences is strongly influenced by the surface properties of the guiding channel. The 3D-printed material exhibits inadequate fluorophobic properties and high surface roughness, rendering it unsuitable for stable droplet processing. Optimal stability of aqueous media droplets embedded in fluorinated oil will be achieved if the channel surface is made of a fluoropolymer material as well. Hence, commercially available PTFE- or FEP-tubings were widely used for stable processing of droplet sequences.[45] To circumvent stability issues within the MTT, the design was made to integrate the PTFE storage tubing end directly into the droplet forming junction, ensuring that droplet are formed directly inside the fluorinated material. To guide both, the inserted PTFE-Tubing as well as the capillary the MTT channels were designed accordingly (see Fig. 2). The precise aspiration of individual objects is determined by both their spatial distribution on the source and the spatial dimension of the tip (see Fig. 2b and f). The extension of the tip is determined by the central uptake channel diameter and the structurally required wall thickness around this channel. The flow at the tip must be sufficient to capture the objects but without damaging the cellular objects or capturing neighbouring cells. To achieve single-object selectivity, it is essential to optimize both the spatial distribution of the objects on the source and the dimensional design of the tip. Additionally, some constructive constrains for the MTT have to be considered to allow imaging of the tip. However, various design iterations were explored to meet all these requirements (see SI, Fig. 2). Due to dimensional limitations of the employed 3D-printing technology, the minimum achievable MTT tip size was approximately 1 mm dimension, with a channel opening for Q_{takup} of about 200 µm diameter (see SI, Fig. 2b). The spatial resolution achievable with this design was inadequate for the precise aspiration of objects in the sub 100 µm range. To enhance spatial resolution, a MTT variant was made with shortened tip and equipped with a 20 mm long fused silica capillary featuring an outer diameter (OD) of 360 µm and an inner diameter (ID) of 100 µm. Final design is shown in Fig. 2a.

Fluidic performance is primarily limited by the pressure drop, media viscosities and the applied flow rates. In microfluidic systems relying on negative pressure for aspiration, the flow rate becomes a critical parameter, as the formation of cavity bubbles will significantly disrupt or even prevent proper processing. Hence, we characterized the capillary MTT carefully for the applicable parameter range. Typical application flow rates were carried out at Q_{out} = 20 µL min^{-1}, Q_{in} = 6–18 µL min^{-1} resulting in 2–14 µL min^{-1} Q_{uptake} flow rates. However, the most consistent droplet formation was always achieved when Q_{in}/Q_{out} is about 1/2. Under these

conditions, regular droplet sequences with low variation were observed.

Workflow and experimental robotic environment

An efficient pick-and-place workflow hinges on process automation, which is essential for achieving consistent performance. To demonstrate the functionality of the MTT, we integrated it into an experimental robotic workflow, as depicted in Fig. 1a–d. Both the MTT and the robotic platform were designed to sort target objects ranging from 20 to 80 μm in size from a 6 cm Petri dish source. For optimal single-object picking, the experimental conditions must ensure that the desired objects are positioned within a defined horizontal plane at the bottom of the Petri dish without adhering to the surface. In the simplest case, dispersed objects settle to the bottom simply by gravity. The use of non-adherent cells, confinement to one plane, and sufficient spacing are essential for our system to achieve accurate imaging, precise robotic positioning, and reliable single-object picking without co-aspiration.

Furthermore, the visibility of the desired objects is paramount, as accurate location and distinction between them are required for reliable hit annotation and selection. Automated single-object recognition and decision-making, utilizing image analysis algorithms, rely heavily on image quality. Both constraints are common to almost all pick-and-place systems.

The experimental setup (see SI, Fig. 1) comprises four main functional modules that are integrated at both the hardware and software levels: **1.) Robotic module:** This module features an *X*–*Y*–*Z* portal positioning system consisting of three linear axes (150 mm each) mounted on a rigid aluminium frame. These axes are connected to a computational control unit for precise movement. The reference *x*, *y*, and *z* coordinates of the MTT tip and the Petri dish were manually teached to the system prior to robotic operation. **2.) Visual feedback system:** A vertically aligned USB-camera installed on the *z*-axis was incorporated to analyse target objects for picking and to capture the position of the MTT-tip, critical for accurate process alignment. The MTT module connects to a two-channel precision syringe pump through PTFE tubing, supplying fluorinated oil for compartmentalization and generating negative pressure for the take-up process. The MTT was also mounted on the *Z*-axis of the system, at an angle closely aligned with the camera. This configuration enables precise positioning above the source objects while providing sufficient space for object recognition. **3.) Carrier stage:** This component was installed onto the *X*–*Y*-axis combination and supports a 60 mm Petri dish containing the target object population. It features a three-point levelling mechanism for fine adjustments of the Petri dish in the horizontal plane. Additionally, it includes various excitation options to optimize illumination conditions. **4.) Control software:** A custom LabVIEW software suite analyses images and coordinates all operational movements and events, streamlining the workflow (see SI, Fig. 3 and 4). **5.) Target support:** For individual placement of the stored droplets onto desired target. The carrier stage can be swapped for a microtiter plate support, which also accommodates wicking paper or other supports.

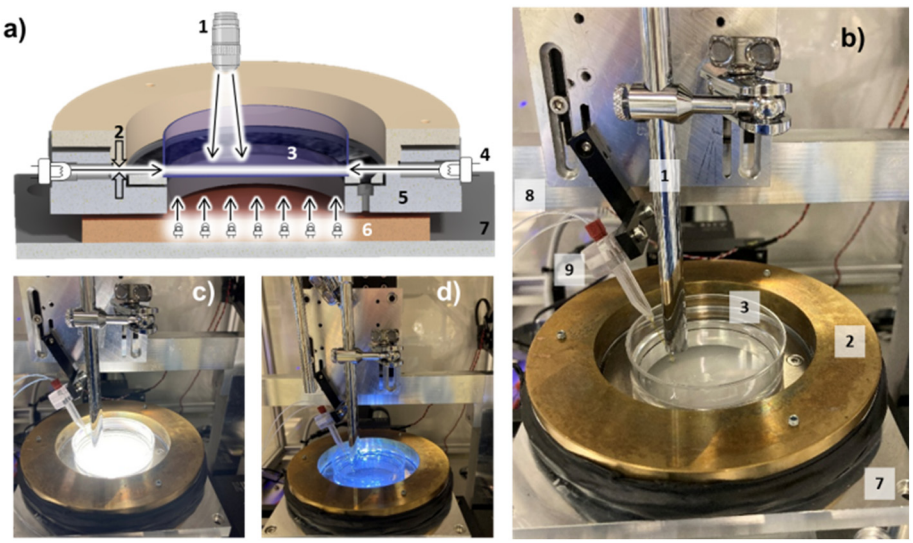

Fig. 3 Excitation and imaging unit of the setup. This figure presents both images and a schematic representation of the source Petri dish setup, supported by a carrier stage including an illumination frame: a) Cross-Sectional Schematic: (1) USB-pen-camera featuring integrated epi-illumination LEDs. (2) Adjustable brass ring for controlling the excitation gap of ring illumination. (3) The 6 cm Petri dish containing the submerged objects. (4) Ring excitation LEDs encircling the Petri dish. (5) levelling frame that supports horizontal adjustment of the Petri dish. (6) Planar LED-array for trans-illumination. (7) Robotic *X*,*Y*-stage for precise positioning. b) Image of fully equipped system: complete robotic system, highlighting the camera (1), Microfluidic Transfer Tool (MTT) (9), storage and fluorinated oil tubing (8), and the source Petri dish (3). c) Trans-illumination mode: object excitation utilizing the planar LED-array (6) for trans-illumination. d) Ring-Gap Excitation Mode: object excitation using the ring-gap excitation mode using blue LEDs (4).

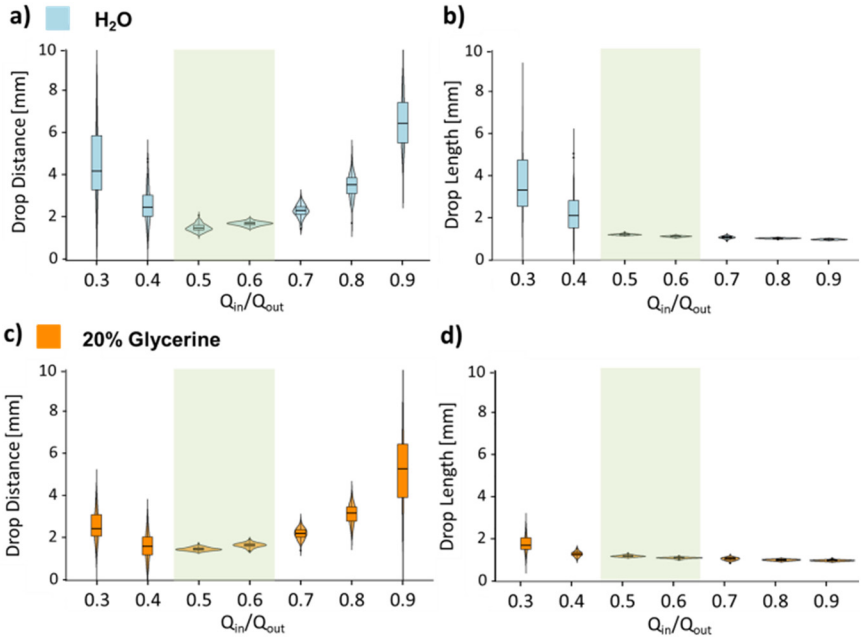

Fig. 4 Statistical analysis of droplet sequence regularity is presented using violin plots: a) and c) droplet distances for varying Q_{in}/Q_{out} ratios; b) and d) droplet length (~volume) for varying Q_{in}/Q_{out} ratios. The mass balance between the actively controlled Q_{out} and Q_{in} flow rates cause the flow rate for takeup ($Q_{out} - Q_{in} = Q_{takeup}$). Experimental data were collected using two representative liquids—water and a 20% glycerin solution—to model commonly used viscous media. Highlighted regions denote the operating conditions associated with the highest droplet and sequence regularity.

Image quality is significantly influenced by the imaging system, which encompasses the camera, objective lenses, and illumination conditions. Biological specimens possess diverse optical properties, necessitating tailored illumination strategies for different object types. For instance, plant cells, seeds, and insect eggs typically display higher contrast under epi-illumination and are often opaque. In contrast, eukaryotic cells, cell aggregates, and spheroid objects are generally translucent, requiring distinct illumination settings for effective recognition and classification. To facilitate optimal lighting adjustments and enhance object contrast, we integrated multiple lighting options into the system (see Fig. 3). In addition to the epi-illumination provided by the pen-camera's integrated LEDs, our setup includes a 10 × 10 cm white-light LED plate for transmission illumination (see Fig. 3c), along with a ring-slit excitation system (see Fig. 3d). The design features 36 LED positions arranged in a circular configuration around the source plate, half fitted with white LEDs and the other half with blue LEDs. To control the 3D radiation profile of these LEDs in two dimensions, we incorporated an adjustable gap mechanism, utilizing a height-adjustable brass ring. By adjusting this ring, the excitation gap can be precisely configured to align with the object plane, effectively accommodating variations in object height. This alignment significantly enhances image quality by ensuring that the illumination plane aligns with the object's plane (see Fig. 3a). The intensity and colour of the excitation light can be further optimized to improve image contrast and reveal finer details. Additionally, polarization filters can be positioned in front of the camera and above the LED array to enable phase-contrast enhancement, allowing for greater clarity in image capture.

The general pick-and-place workflow as illustrated in Fig. 1a–d involves the following procedural steps after experiment setup: **1.) Image analysis and object identification:** The imaging field is analysed to identify target objects based on predefined size or colour selection criteria. Object recognition was performed using a standard procedure consisting of contrast optimization, R,G,B-value splitting, image binarization, and subsequent area-size–based recognition. The object coordinates were determined by calculating the *x*–*y* travel distance from a previously defined reference position. **2.) Positioning and path calculation:** The positional coordinates of the selected objects are stored, and a pickup path for the MTT-tip calculated. To minimize the risk of collecting undesired nearby objects, only isolated hits with at least 200 μm of free space surrounding them are scheduled for pickup. The required free space parameter was not optimized, as successful single-object pickup is primarily determined by the spatial distribution of the objects. Therefore, object dilution was adjusted visually by dilution, and the free space parameter was simply set to four times the object size. **3.) Aspirating and compartmentalizing:** The positionally calibrated *XYZ* stage moves the MTT tip along the calculated path while continuously aspirating. Controlled retention at the target location, combined with precise *z*-axis adjustment of the MTT tip, ensures a high uptake rate of only the desired objects. Inside the MTT, the aspirated volume is compartmentalized with fluorinated oil. To maintain a constant aspiration flow rate (Q_{takeup}) during pickup, the time needed to aspirate one object and move to the next one was aligned with the droplet formation frequency. This supports the collection of a single object per droplet generation interval. The resulting

sequence separates the picked objects into individual droplets, which are stored in PTFE-tubing between the MTT and syringe pump. The about 80 cm length and 0.5 mm inner diameter of the tubing limit the total number of storable droplets to maximal 400 per run. **4.) Next target identification:** The camera analyses the imaging field, displaying the MTT tip along with several objects, to identify the next target hits and recalculate the pickup path. The MTT scans the Petri dish in a meandering motion, collecting all objects identified as hits within the imaging area. **5.) Placement phase:** In the placement phase, fluid actuation is halted, and the MTT tip is lifted to complete the picking process. After replacing the source Petri dish with a new target, the MTT is lowered to the target level, and the previously stored droplet sequence is dispensed in a defined, sequential manner. Two operation modes are employed during dispensing: surface-based deposition onto materials such as agar, polymers, or wicking substrates like paper, and submerged dispensing into pre-filled microtiter plate wells or other containers. The dispensing flow rate and *X*, *Y*, *Z* positioning are adjusted according to the chosen mode. Consequently, both the droplet-embedded objects and the separating fluorinated oil are deposited onto the target surface or into the target wells. In surface deposition mode, hydrophilic materials enhance the uniform distribution of the deposited objects.

Results and discussions

Fluidic characterization of the MTT

The fluidic characteristics of the MTT are primarily determined by the pressure drop across the fused silica capillary and the viscosity of the aspirated medium. Droplet formation is predominantly influenced by the geometry of the droplet-forming junction and the ratios of the applied flow rates. A critical quality metric is the regularity of the droplet sequence, particularly with regard to consistent droplet length and spacing. For the MTT equipped with capillary (length = 20 mm, inner diameter = 100 μm), we measured the pressure drop across a 50 cm segment of PTFE tubing (outer diameter = 1/32″, inner diameter = 0.5 mm) at flow rates up to 100 μL min^{-1} at 21 °C. The pressure drop is affected by two fluids: water (viscosity = 1.0 mm^2 s^{-1}) and fluorinated oil (PP9, viscosity = 3.25 mm^2 s^{-1}), the latter being used for pressure drop measurement due to its higher viscosity, which provides a broader range of applicable fluids. Based on the pressure drop, the fluidic resistance coefficients have been calculated. The resulting fluidic resistance coefficients are provided in SI-Table 1. The operational flow rates for pickup and placement modes are approximately 10 μL min^{-1} and 30 μL min^{-1}, respectively. In both scenarios, the pressure drop remains well below 200 mbar, a level easily managed by the attached syringe pumps. However, in aspiration mode microfluidics, ensuring a proper and bubble-free initialization of the MTT is critical for reliable operation.

The quality of droplet formation at the MTT junction was evaluated using a light barrier sensor positioned on the storage tubing near the MTT. The integrity of the droplet sequence is reflected in the temporal absorption signal. Variations in flow rates and media lead to differences in droplet length and spacing. The balance of active controls between the outlet flow rate (Q_{out}) and the inlet flow rate (Q_{in}) generates the effective uptake flow rate (Q_{takeup}), meaning that fluctuations in Q_{in} at a constant Q_{out} alter the Q_{in}/Q_{takeup} ratio, consequently affecting the droplet sequence. Two different viscosities were tested during aspiration: pure water (1.0 mm^2 s^{-1}) and a 20% aqueous glycerine solution (2.0 mm^2 s^{-1}). The inlet flow rate (Q_{in}) was varied between 30% (6 μL min^{-1}) and 90% (18 μL min^{-1}) of the outlet flow rate (Q_{out}), which was held constantly at 20 μL min^{-1}. SI Video S1 illustrates the MTT during continuous aspiration and droplet formation process. To ensure statistical significance, approximately 100 droplets were analysed for each condition. Results, shown in Fig. 4, indicate that the highest droplet regularity—largely independent of fluid viscosity—was achieved when Q_{in} was maintained at 50% to 60% of Q_{out}. However, when Q_{in} exceeded 65% of Q_{out}, the spacing between droplets decreased significantly, leading to irregularity, although the droplet length remained unaffected. These findings demonstrate that the droplet-forming junction is robust and capable of producing consistent droplets, even when flow rates or viscosities vary within the tested range.

Benchmarking object sorting using the MTT

The effectiveness of a morphology-based pick-and-place screening process is influenced by several factors, as previously discussed. Traditional systems are primarily constrained by the limitation of moving only one identified hit per cycle. To demonstrate the advantages of an enhanced operational mode —utilizing sequential pickup with intermediate storage of selected "hit" objects before their eventual placement—an appropriate model assay must be chosen. Developing cell assays based on morphological changes necessitates a solid understanding of cell culture techniques and thorough preparations prior to selection operations. The same considerations apply to the subsequent monitoring of selected hits to assess their developmental morphology. However, the most critical step following the morphology-based selection remains the "pick-and-place" translocation, which operates independently of the optical decision-making process. Additionally, the current imaging system has limitations regarding resolution and optical magnification.

To evaluate MTT performance effectively, we selected a model system featuring fluorescent beads of varying sizes and colours for sorting. Specifically, we mixed three types of fluorescent polymer particles: (1) blue-fluorescent particles with diameters of 45–53 μm, (2) green-fluorescent particles measuring 53–63 μm, and (3) red-fluorescent particles with a diameter of 48 μm. These particles were dispersed in an aqueous medium containing 0.12% SDS surfactant, chosen to mimic the surfactant properties of typical cell culture

media—which can interfere with droplet generation—and to reduce adhesion forces among the particles. The particle dispersion was introduced into the source Petri dish, which was then placed on a horizontally aligned carrier stage with the liquid level adjusted to approximately 2 mm. The particle density was calibrated to around 10 particles per mm^2. Given the surface area of the 60 mm Petri dish ($(30\ mm)^2 \times \pi \approx 2.827\ mm^2$), the source population contained roughly 28 000 particles. To ensure uniform particle distribution, meticulous aspiration and dispensing using a pipette were performed. For particle selection, a particle-free radius of approximately 200 μm around each targeted particle was established in the software. However, as with all pick-and-place systems, the single-event picking rate depends significantly on the careful optimization of this parameter. The system was configured to sort the source population into distinct particle classes based on colour or diameter. The number of objects selected was limited to 300, dictated by the storage tubing's length.

Fig. 5 illustrates an image sequence of the selection area as recorded by the system camera. For demonstration purposes, the MTT tip was programmed to return to its starting position after selecting the target particles. The images on the left (a, c, e) depict the initial particle distribution, while the images on the right (b, c, d) show the same area after aspiration of the targeted particles. Upon closer examination, it is evident that the movement of the MTT tip across the source population results in only negligible displacements of non-target particles. The pickup movement involves an initial Z-lift of approximately 100 μm, followed by linear *X*–*Y* translation to the next target position, and concludes with a *Z*-lower movement. Furthermore, the images confirm that the defined 200 μm particle-free radius enables precise single-particle selection without inadvertently aspirating nearby particles.

To count the droplets containing embedded particles in the storage tubing, a microscope camera was positioned to capture images of the droplet storage area near the MTT. Multiple picking runs were conducted and the number of objects per droplet was analysed through video analysis (see SI Video S6). Fig. 6a and b presents typical images of the storage droplets with embedded objects. The camera's field of view was adjusted to clearly visualize individual droplet transitions, and the resulting video analysis quantified the number of objects per droplet picked up from the source (see SI Video S6). Approximately 200–350 droplets from different runs were analysed. The results, illustrated in Fig. 6c and d, reveal that about 60% of the stored droplets contained a

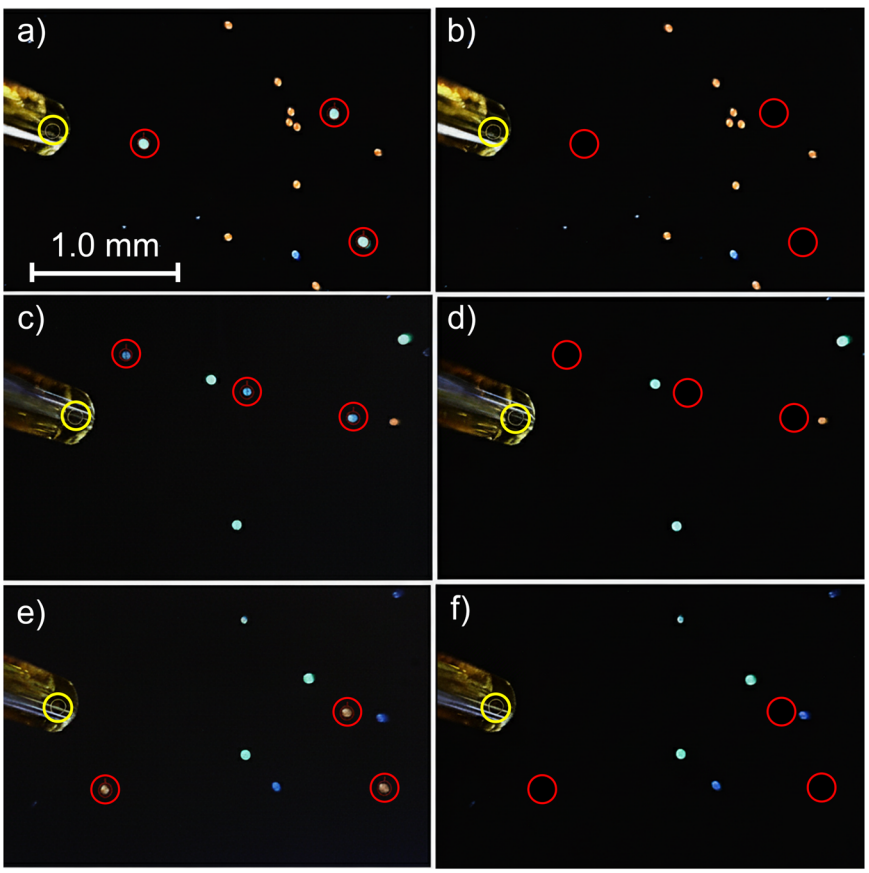

Fig. 5 Image comparison before and after the picking process. The images on the left (a, c and e) illustrate the particle field, with colour-selected particles marked by red circles indicating 200 μm diameter particle free space. The yellow circle indicates the position of the MTT capillary orifice, which is programmed to return to its initial position after picking the highlighted objects. The right-hand images (b, d and f) show the same field after selection, demonstrating that the colour-selected particles are no longer present (see SI Video S2 to S5).

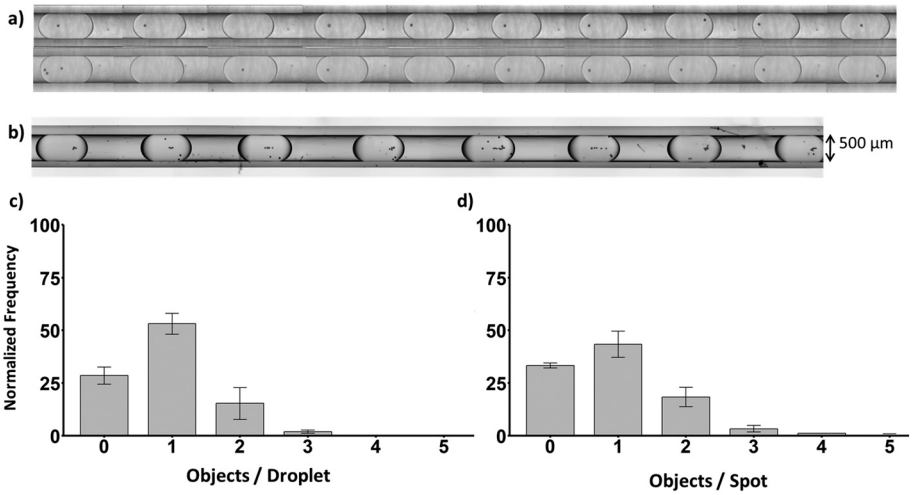

Fig. 6 Microscope images of the storage tubing with droplet encapsulated objects. a) Optimized conditions for single object picking (images arrayed from video stream). b) Statically occupied droplets received by random aspiration with non-optimized conditions (image taken with external digital-imaging system) tube ID: 500 µm. c) Obtained object frequency inside the droplets after aspiration (N = 350) d) obtained object frequency after re-placement onto a wicking paper surface (N = 3 × 80 = 240).

single object, while roughly 33% were empty and only 5% contained two objects. Failed picking occurs if the initially identified object is no longer at its expected position for any reason, or if it adheres to the surface, preventing that the fluid stream Q_{takeup} can take it up. Notably, droplets with more than two objects accounted for less than 1%. This distribution of occupancy is primarily influenced by the spatial arrangement of particles in the source and provides limited insight into the MTT's encapsulation performance. A carefully prepared setup featuring a highly diluted particle population in the source ensures that all particles are adequately spaced, minimizing adjacent particles. In optimal conditions, this spacing can lead to a 100% single occupancy rate in the droplet sequence. Achieving this ideal scenario may involve using structured sources that define the location of the objects.

It is important to note that multiple objects can be aspirated if required by an assay protocol. Conversely, in situations where particle density is high or when dispersed objects are used as the source, multiple objects can also be aspirated and stored within the droplets. In such cases, the number of encapsulated objects per droplet will be determined statistically. By optimizing the particle density in the source, the potential for multi-object occupancy can be adjusted to align with specific assay requirements. Fig. 6b depicts a representative example of a dense particle population aspirated from a settled layer in the Petri dish, where the particle density was approximately 100 objects per mm^2.

To complete the full pick-and-place process, temporarily stored objects must be accurately transferred to the target location. Two operational modes are available: a) dispensing droplets onto a surface and b) dispensing them into a liquid medium. In both scenarios, the presence of fluorinated oil must be considered. While most assays can tolerate this inert material, its impact on the deposition process must be acknowledged. In surface-mediated placement, the adhesion behaviour is influenced by the surface tension among the target surface, the aqueous droplets, and the fluorinated oil. Agar-based media and other polar surface materials typically facilitate good adhesion for the object-containing droplets. However, the dispersion of fluorinated oil around the aqueous droplets necessitates wider spacing between individual target locations. Generally, the spacing between dispensing sites ranges from 1 to 5 mm, driven by the requirements of subsequent processes. We tested several target surfaces: agar with 9 mm spacing, microtiter plate lids with 9 mm spacing, and paper-based targets with 4.5 mm spacing (see Fig. 7). In all cases, droplets containing objects were successfully transferred onto the surfaces with 100% efficiency. However, reliably identifying the placed objects within the sessile droplets—especially when potentially obscured by fluorinated oil—can be challenging due to reflections and optical refraction. To address this issue, we selected a wicking paper surface as the target. This design enhances visibility by drawing away liquids, allowing for easy counting of the remaining objects on the surface to assess placement success. Fig. 7 illustrates the various targets: a) shows placed objects on the wicking paper surface, while b) displays sessile droplets on a microtiter plate lid. Details are given in the SI Video S7.

Repetitive analysis of 80 paper spots (16 × 5 arrangement) revealed particle occupancy similar to that observed in the storage droplets (see Fig. 6). This consistency suggests that once objects are aspirated, they are reliably encapsulated within droplets, indicating that the occurrence of double or multiple-occupied droplets arises from parallel uptake rather than mixing within the MTT. When the picked objects need to be transferred into a liquid medium, a pre-filled microtiter plate (MTP) serves as the target. In this scenario, the MTT tip must be submerged

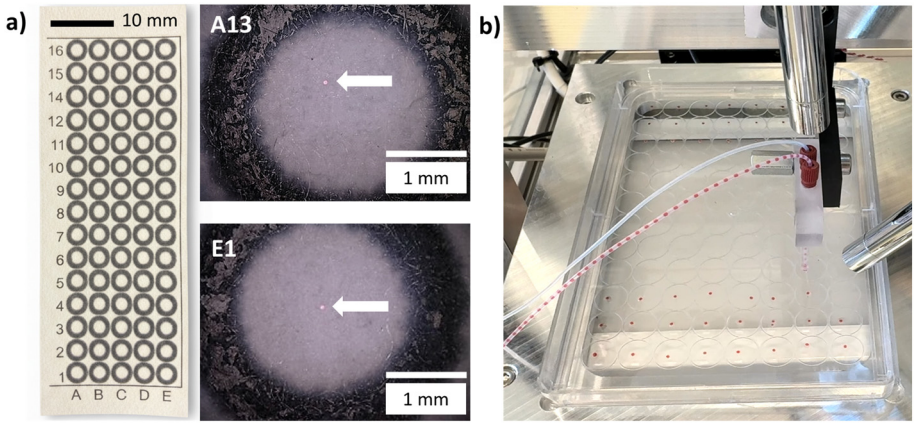

Fig. 7 Images of targets for place operation. a) Used wicking paper array with magnified spots of placed particles. Circular markers and identifiers were printed by laser printer. **A13/E1** images of the corresponding position indicating deposited objects. b) 96-Well microtiter plate lid with placed droplets (red colored media).

in the target liquid. Due to its high density (~2 g mL^{-1}), the dispensed fluorinated oil detaches from the tip and sinks to the bottom of the well, allowing the object-containing droplets to mix with the fresh medium and release the encapsulated objects. Notably, the operational demands for placing droplets are significantly less than for selectively picking the objects. Various runs were conducted to assess different selection criteria. In case of the investigated colour-based selection, the achieved single-object transfer rate was approximately 60–70%, with 20–30% empty spots remaining after transfer. The transfer of 80 objects onto the wicking surface array required about 90 sec. Similar performance was achieved when using the 96-well plate lid as the target (see Fig. 7b), with an overall transfer time of approximately 100 s. Neglecting the time potentially required for target plate replacement, approximately 300

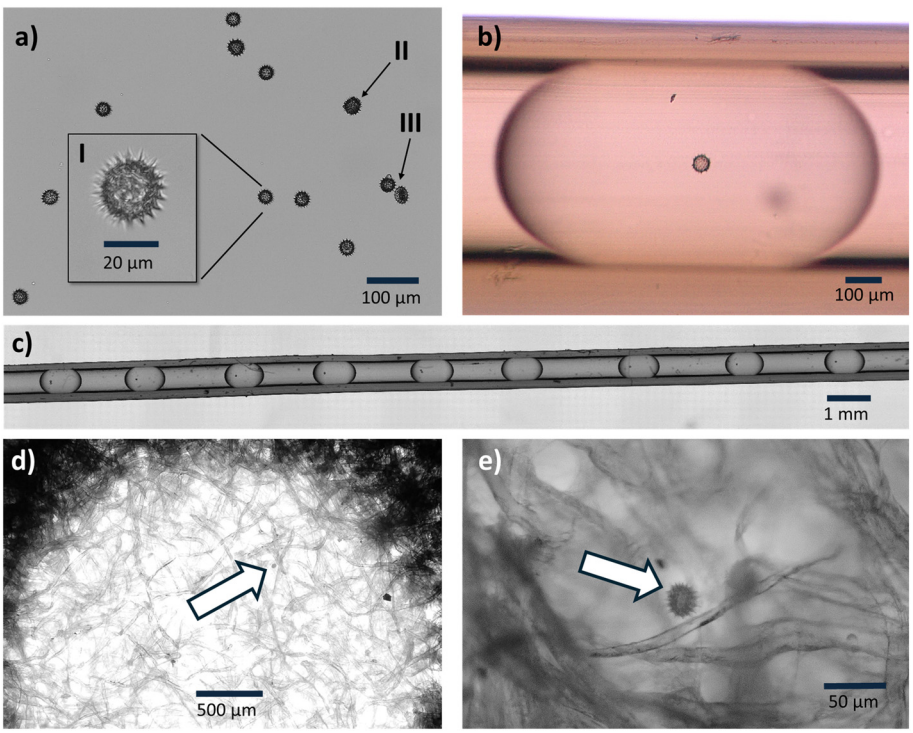

Fig. 8 Exemplary sorting of *Helianthus annuus* pollen in hydrated state. a) Pollen source population of about 20 µm diameter dispersed in the Petri dish. A combined image-based selection criteria section for object area of 300–320 μm^2 (19.5–20.2 µm diameter) and an object circularity of 0.9 to 1.0 were used. Inset **I** meets both criteria, **II** oversized pollen, **III** malformed pollen. b) Exemplary droplet embedded pollen inside the intermediate storage tubing after picking. c) Microscopic image of the droplet storage sequence occupied with selected pollen. d) Image of the placed pollen after dispensing the stored dropets onto a wicking paper as shown in Fig. 7. e) Magnification of a pollen on paper surface.

objects (limit of used intermediate storage tube) can be transferred in about 300 s under optimized conditions.

Biological application and constrains

We demonstrated the applicability of the overall system with pollen isolated from sunflower (*Helianthus annuus*) inflorescences by blending in culture buffer, centrifugation and filtration through 63 μm filter. These pollen grains possess a hedgehog-like surface structure and exhibit a hydrated diameter of approximately 20 μm. The pollen sample was dispersed in a 1% glycerine-buffered solution and transferred into the source Petri dish. Compared to polymeric particles, the optical properties of pollen are more challenging due to their faint yellowish, partially transparent appearance. Nevertheless, after optimization of the excitation conditions, the pollen were image-based sorted according to an object area of 300–320 μm^2 (corresponding to a diameter of 19.5–20.2 μm) and a circularity between 0.9 and 1.0 (see SI). A wicking paper target was used, and the stored droplet sequence was dispensed into array positions (see Fig. 8a). Microscopic analysis of droplet occupation in the intermediate storage tube and on the target array was performed only on a spot-check basis. The resulting images are summarized in Fig. 8. The single-transfer rates obtained for the 20 μm pollen were comparable to those observed with 50 μm polymeric beads. The system may also be applied to other mammalian and plant cell types of different sizes. However, successful application requires careful consideration of system prerequisites, optical and fluidic boundary conditions, and cell-specific culture requirements. From a technical perspective, single-object picking of cell types smaller than 20 μm may be limited by optical detection, surface adhesion, or multiple-picking events caused by unfavourable cell distributions in the source. Furthermore, mechanical, thermal, and oxygen-related stress must be taken into account during cell picking, storage, and placement. For particularly sensitive cells, the time required for manipulation should be minimized to reduce stress. In this regard, our improved transfer workflow may provide a distinct advantage. Altogether, these factors are critical for preserving cell integrity and viability during sequential droplet-based single-cell handling.

Conclusions

The goal of this work was to enhance the process performance of image-based pick-and-place operations through the incorporation of droplet-based intermediate storage. To achieve this, we developed a Microfluidic Transfer Tool (MTT) capable of selectively picking up dispersed objects of about 20–50 μm in diameter and encapsulating them into nanoliter-sized droplets. This innovative approach allows multiple objects to be picked up and stored sequentially in droplets, thereby significantly minimizing the number of source-to-target transfer operations required. To validate the advantages of this methodology, we constructed an experimental robotic setup equipped with a multipurpose excitation stage and a pen-camera for imaging. Object recognition and classification were facilitated by algorithmic criteria based on colour, size, or shape. To benchmark the system and workflow, we successfully sorted a mixed sample of coloured polymeric particles. Finally, the technology was successfully applied to biological sample, enabling the sorting of 20 μm hits from *Helianthus salicifolia* pollen population.

The results demonstrated that approximately 300 classified objects were transferred into individual microtiter plate wells in about 5 minutes. In contrast, a one-to-one transfer operation, requiring about 20 seconds per object, would take 20 seconds × 300 objects = 6000 seconds, or 100 minutes. Comparing these conditions, the overall process time is reduced by a factor of about 20. Thus, implementing the MTT significantly reduces the overall processing time, showcasing its potential to enhance the efficiency of image-based pick-and-place operations. The successful sorting of about 20 μm plant pollen by size and shape demonstrates the workflow's versatility and broad applicability.

Author contributions

AG, JC: PIs, conceptualization & methodology. MD, JB, OD, QY: resources, OG, JC, RW: data curation & investigation, MK, KP: funding acquisition & project administration, SS: software, AG, JC: supervision, OG, JC, AG: writing – original draft.

Conflicts of interest

Authors declare no conflicts of interests.

Data availability

Supplementary data, including videos, are provided to illustrate additional details of the system, software, and results. The supplementary videos demonstrate the functionality and effectiveness of the Microfluidic Transfer Tool (MTT), offering a clearer understanding of the pick-and-place process. Supporting images show further details of the robotic setup and examples of polymer particles placed onto a wicked paper surface. The CAD file of the MTT design used for 3D printing is also included in STEP-format.

Supplementary information: supporting data and videos are available see supplementary information (SI). See DOI: https://doi.org/10.1039/d5lc00550g.

Acknowledgements

The authors gratefully acknowledge financial support from the Allianz für Industrie und Forschung (AiF) through the ZIM program, project "μProPlant" (FKZ: KK5240405AJ2) and partially support from the "Bund-Länder Tenure-Track Program" of the Federal Ministry of Education and Research (BMBF; FKZ.: 16TTP133). Helpful support and discussions from Prof. Dr. Steffen Strehle and Mr. Paul Bucklitsch (Dept. Microsystem-Engineering) is gratefully acknowledged.

Notes and references

1 M. Esner, F. Meyenhofer and M. Bickle, Live-Cell High Content Screening in Drug Development, *Methods Mol. Biol.*, 2018, **1683**, 149–164.

2 D. Feldman, L. Funk, A. Le, R. J. Carlson, M. D. Leiken, F. Tsai, B. Soong, A. Singh and P. C. Blainey, Pooled genetic perturbation screens with image-based phenotypes, *Nat. Protoc.*, 2022, **17**, 476–512.

3 D. Krentzel, S. L. Shorte and C. Zimmer, Deep learning in image-based phenotypic drug discovery, *Trends Cell Biol.*, 2023, **33**, 538–554.

4 D. Kusumoto, T. Seki, H. Sawada, A. Kunitomi, T. Katsuki, M. Kimura, S. Ito, J. Komuro, H. Hashimoto, K. Fukuda and S. Yuasa, Anti-senescent drug screening by deep learning-based morphology senescence scoring, *Nat. Commun.*, 2021, **12**, 257.

5 S. Lin, K. Schorpp, I. Rothenaigner and K. Hadian, Image-based high-content screening in drug discovery, *Drug Discovery Today*, 2020, **25**, 1348–1361.

6 I. Lukonin, M. Zinner and P. Liberali, Organoids in image-based phenotypic chemical screens, *Exp. Mol. Med.*, 2021, **53**, 1495–1502.

7 C. E. Mills, K. Subramanian, M. Hafner, M. Niepel, L. Gerosa, M. Chung, C. Victor, B. Gaudio, C. Yapp, A. J. Nirmal, N. Clark and P. K. Sorger, Multiplexed and reproducible high content screening of live and fixed cells using Dye Drop, *Nat. Commun.*, 2022, **13**, 6918.

8 X. Li, X. Liang, J. Yin and W. Lin, Organic fluorescent probes for monitoring autophagy in living cells, *Chem. Soc. Rev.*, 2021, **50**, 102–119.

9 T. Terai and T. Nagano, Small-molecule fluorophores and fluorescent probes for bioimaging, *Pflügers Arch.*, 2013, **465**, 347–359.

10 H. Zhu, J. Fan, J. Du and X. Peng, Fluorescent Probes for Sensing and Imaging within Specific Cellular Organelles, *Acc. Chem. Res.*, 2016, **49**, 2115–2126.

11 A. J. Lam, F. St-Pierre, Y. Gong, J. D. Marshall, P. J. Cranfill, M. A. Baird, M. R. McKeown, J. Wiedenmann, M. W. Davidson, M. J. Schnitzer, R. Y. Tsien and M. Z. Lin, Improving FRET dynamic range with bright green and red fluorescent proteins, *Nat. Methods*, 2012, **9**, 1005–1012.

12 R. N. Day and M. W. Davidson, The fluorescent protein palette: tools for cellular imaging, *Chem. Soc. Rev.*, 2009, **38**, 2887–2921.

13 F. Richter, M. Chen, P. Schaub, F. Wüst, D. Zhang, S. Schneider, G. A. Groß, P. Mäder, O. Dovzhenko, K. Palme, J. M. Köhler and J. Cao, Induction of embryogenic development in haploid microspore stem cells in droplet-based microfluidics, *Lab Chip*, 2022, **22**, 4292–4305.

14 T. Bonnefoix, P. Bonnefoix, P. Verdiel and J. J. Sotto, Fitting limiting dilution experiments with generalized linear models results in a test of the single-hit Poisson assumption, *J. Immunol. Methods*, 1996, **194**, 113–119.

15 D. J. Collins, A. Neild, A. deMello, A.-Q. Liu and Y. Ai, The Poisson distribution and beyond: methods for microfluidic droplet production and single cell encapsulation, *Lab Chip*, 2015, **15**, 3439–3459.

16 Y. Zhou, D. Shaw, C. Lam, J. Tsukuda, M. Yim, D. Tang, S. Louie, M. W. Laird, B. Snedecor and S. Misaghi, Beating the odds: The poisson distribution of all input cells during limiting dilution grossly underestimates whether a cell line is clonally-derived or not, *Biotechnol. Prog.*, 2018, **34**, 559–569.

17 Biotron Healthcare, Biotron Healthcare Automated Single Cell Picking System, https://www.biotronhealthcare.com/automated-single-cell-picking-system/, (accessed 24 February 2025).

18 MMI CellEctor, Molecular Machines & Industries Cell Picking Technology, https://www.molecular-machines.com/products/cell-picker, (accessed 6 February 2025).

19 Satorius, Single Cell, Clone & Colony Analysis, Screening & Isolation, https://www.sartorius.com/en/products/cell-selection-and-retrieval/cell-selection-instruments, (accessed 19 May 2025).

20 Shimadzu CellPicker, Automated Pick and Collection Tool of Cell Colonies, https://www.shimadzu.com/an/products/life-science-lab-instruments/cell-research/cell-picker/index.html, (accessed 19 May 2025).

21 M. T. Guo, A. Rotem, J. A. Heyman and D. A. Weitz, Droplet microfluidics for high-throughput biological assays, *Lab Chip*, 2012, **12**, 2146–2155.

22 T. Moragues, D. Arguijo, T. Beneyton, C. Modavi, K. Simutis, A. R. Abate, J.-C. Baret, A. J. deMello, D. Densmore and A. D. Griffiths, Droplet-based microfluidics, *Nat. Rev. Methods Primers*, 2023, **3**, 32.

23 J. Clausell-Tormos, D. Lieber, J.-C. Baret, A. El-Harrak, O. J. Miller, L. Frenz, J. Blouwolff, K. J. Humphry, S. Köster, H. Duan, C. Holtze, D. A. Weitz, A. D. Griffiths and C. A. Merten, Droplet-based microfluidic platforms for the encapsulation and screening of Mammalian cells and multicellular organisms, *Chem. Biol.*, 2008, **15**, 427–437.

24 E. K. Sackmann, A. L. Fulton and D. J. Beebe, The present and future role of microfluidics in biomedical research, *Nature*, 2014, **507**, 181–189.

25 S. Mashaghi, A. Abbaspourrad, D. A. Weitz and A. M. van Oijen, Droplet microfluidics: A tool for biology, chemistry and nanotechnology, *TrAC, Trends Anal. Chem.*, 2016, **82**, 118–125.

26 J. M. Köhler and B. P. Cahill, *Micro-Segmented Flow*, Springer, Berlin Heidelberg, Berlin, Heidelberg, 2014.

27 J. Cao, C. Chande and J. M. Köhler, Microtoxicology by microfluidic instrumentation: a review, *Lab Chip*, 2022, **22**, 2600–2623.

28 R. Mazetyte, K.-P. Kronfeld and J. M. Köhler, Five-Level Structural Hierarchy: Microfluidically Supported Synthesis of Core–Shell Microparticles Containing Nested Set of Dispersed Metal and Polymer Micro and Nanoparticles, *Part. Part. Syst. Charact.*, 2023, **40**, DOI: 10.1002/ppsc.202300030.

29 H. A. Phan, K. Nguyen, P. T. Pham, L. D. Quang, H. B. Thu, D. B. Lam, C.-P. Jen, T. B. Thanh and T. C. Duc, On-demand electrostatic droplet sorting and splitting, *Sens. Actuators, A*, 2025, **385**, DOI: 10.1016/j.sna.2025.116311.

30 S. Köster, F. E. Angilè, H. Duan, J. J. Agresti, A. Wintner, C. Schmitz, A. C. Rowat, C. A. Merten, D. Pisignano, A. D. Griffiths and D. A. Weitz, Drop-based microfluidic devices for encapsulation of single cells, *Lab Chip*, 2008, **8**, 1110–1115.

31 J. Panwar, A. Autour and C. A. Merten, Design and construction of a microfluidics workstation for high-throughput multi-wavelength fluorescence and transmittance activated droplet analysis and sorting, *Nat. Protoc.*, 2023, **18**, 1090–1136.

32 A. Autour and C. A. Merten, Fluorescence- activated droplet sequencing (FAD- seq) directly provides sequences of screening hits in antibody discovery, *Proc. Natl. Acad. Sci. U. S. A.*, 2024, **121**, DOI: 10.1073/pnas.2405342121.

33 S. Lindstrom and H. Andersson-Svahn, Overview of single-cell analyses: microdevices and applications, *Lab Chip*, 2010, **10**, 3363–3372.

34 E. J. Medcalf, M. Gantz, T. S. Kaminski and F. Hollfelder, Ultra-High-Throughput Absorbance-Activated Droplet Sorting for Enzyme Screening at Kilohertz Frequencies, *Anal. Chem.*, 2023, **95**, 4597–4604.

35 F. Gielen, R. Hours, S. Emond, M. Fischlechner, U. Schell and F. Hollfelder, Ultrahigh-throughput-directed enzyme evolution by absorbance-activated droplet sorting (AADS), *Proc. Natl. Acad. Sci. U. S. A.*, 2016, **113**, E7383–E7389.

36 J.-C. Baret, O. J. Miller, V. Taly, M. Ryckelynck, A. El-Harrak, L. Frenz, C. Rick, M. L. Samuels, J. B. Hutchison, J. J. Agresti, D. R. Link, D. A. Weitz and A. D. Griffiths, Fluorescence-activated droplet sorting (FADS): efficient microfluidic cell sorting based on enzymatic activity, *Lab Chip*, 2009, **9**, 1850–1858.

37 H.-D. Xi, H. Zheng, W. Guo, A. M. Gañán-Calvo, Y. Ai, C.-W. Tsao, J. Zhou, W. Li, Y. Huang, N.-T. Nguyen and S. H. Tan, Active droplet sorting in microfluidics: a review, *Lab Chip*, 2017, **17**, 751–771.

38 E. Zang, S. Brandes, M. Tovar, K. Martin, F. Mech, P. Horbert, T. Henkel, M. T. Figge and M. Roth, Real-time image processing for label-free enrichment of Actinobacteria cultivated in picolitre droplets, *Lab Chip*, 2013, **13**, 3707–3713.

39 J. M. Lee, M. Zhang and W. Y. Yeong, Characterization and evaluation of 3D printed microfluidic chip for cell processing, *Microfluid. Nanofluid.*, 2016, **20**, DOI: 10.1007/s10404-015-1688-8.

40 J. M. Zhang, A. A. Aguirre-Pablo, E. Q. Li, U. Buttner and S. T. Thoroddsen, Droplet generation in cross-flow for cost-effective 3D-printed "plug-and-play" microfluidic devices, *RSC Adv.*, 2016, **6**, 81120–81129.

41 N. Bhattacharjee, A. Urrios, S. Kang and A. Folch, The upcoming 3D-printing revolution in microfluidics, *Lab Chip*, 2016, **16**, 1720–1742.

42 J. Zhang, W. Xu, F. Xu, W. Lu, L. Hu, J. Zhou, C. Zhang and Z. Jiang, Microfluidic droplet formation in co-flow devices fabricated by micro 3D printing, *J. Food Eng.*, 2021, **290**, 110212.

43 K. C. Lowe, Perfluorochemical respiratory gas carriers: benefits to cell culture systems, *J. Fluorine Chem.*, 2002, **118**, 19–26.

44 https://www.3dsystems.com, 3D-Systems PolyJet MJP-2500-IC.

45 J. Cao, F. Richter, M. Kastl, J. Erdmann, C. Burgold, D. Dittrich, S. Schneider, J. M. Köhler and G. A. Groß, Droplet-Based Screening for the Investigation of Microbial Nonlinear Dose-Response Characteristics System, Background and Examples, *Micromachines*, 2020, **11**, DOI: 10.3390/mi11060577.